GPS MULTI-RECEIVER DIRECT POSITION ESTIMATION FOR AERIAL APPLICATIONS

BY

ARTHUR HSI-PING CHU

THESIS

Submitted in partial fulfillment of the requirements
for the degree of Master of Science in Electrical and Computer Engineering
in the Graduate College of the
University of Illinois at Urbana-Champaign, 2018

Urbana, Illinois

Adviser:

Assistant Professor Grace Xingxin Gao

ABSTRACT

Modern aviation safety increasingly depends on reliable GPS services, while signal degrading effects such as multipath and masking often occur during critical flight phases, such as take-off and landing. In this regard, we propose Multi-Receiver Direct Position Estimation (MR-DPE), which operates a network of DPE receivers to enhance GPS measurement certainty in degraded signal environments. A DPE receiver directly estimates navigation solutions in the PVT domain with a maximum-likelihood approach, bypassing the intermediate range measurements. Whereas prior works have shown the enhanced measurement certainty of DPE under weak signals, MR-DPE provides further improvement by leveraging the information redundancy and the geometric diversity provided by the network of receivers and antennas. We implemented MR-DPE using software-defined radio and conducted comprehensive, full-scale flight experiments, a first for DPE-related works. A wide range of flight profiles were explored, especially those prone to signal multipath and masking, and preliminary analyses were performed on the data collected to ensure the conceptual validity of MR-DPE.

To my parents, for their grace and character.

ACKNOWLEDGMENTS

I would like to express my heartfelt gratitude to my adviser, Professor Grace Xingxin Gao. Her dedication to research and to her students has been a constant inspiration, and I benefited immensely from her guidance, wisdom and patience. I would also like to thank my academic adviser, Professor Jonathan J Makela, who has mentored me with his wealth of knowledge and his exemplary gentleness.

Our research group members, past and present, have never hesitated to come to my aid, and I will always be indebted to them for their camaraderie. They are Mr Craig C Babiarz, Ms Sri Ramya Bhamidipati, Mr Shubhendra VS Chauhan, Mr Derek Chen, Mr Ashwin V Kanhere, Mr Enyu Luo, Ms Tara Y Mina, Ms Yuting Ng, Mr Matthew J Peretic, Mr Akshay P Shetty, Mr Siddharth Tanwar, Mr John J Vergere and Ms Cara Yang.

The flight test described in this thesis was funded and executed under "Project GRIFFIN", a Test Management Project by United States Air Force Test Pilot School, Edwards AFB, CA. I had the pleasure and privilege to work with the GRIFFIN team: Flt Lt Alexander G Blackstock (RAF), Capt Mark S Brodie, Maj Joseph DeMonte IV, Maj Patrick J Highland and Maj John P Wilder. They are truly our nation's finest, and their trust and support throughout the project means all the world to me.

Last but not least, I would like to thank Dr Vladimir I Sotnikov, Mr Nathan E Zechar, Mr James E Caplinger, Mr Andrew Hamilton and Mr Jeffery Unroe of Air Force Research Laboratory Sensors Directorate (AFRL/RYMH) for their kindness and their friendship.

The research covered in this thesis is funded by Air Force Research Laboratory Sensors Directorate (AFRL/RYWN), Wright-Patterson AFB, OH, under contract FA9453-15-1-0075.

This report was prepared as an account of work sponsored by an agency of the United States Government. Neither the United States Government

iv

TABLE OF CONTENTS

CHAPTER 1

INTRODUCTION

Global Positioning System (GPS), with its worldwide coverage [1] and its infrequent need for receiver calibration, has found widespread application acceptance in the aviation community [2, 3]. Conventional receiver architectures, such as the scalar tracking loop (STL) [4, 5] and the vector tracking loop (VTL) [6], are based on the *two-step approach*. That is, a receiver measures its ranges to the visible GPS satellites before triangulating a position-velocity-time (PVT) solution.

Popular for its simplicity and its proven service record, this two-step approach is nonetheless vulnerable in degraded signal environments [7]. More specifically, during episodes of signal multipath [8–10] or signal masking [11, 12], the signal-to-noise ratio (SNR) is reduced, rendering the range measurements unreliable or undetectable. These degrading effects often occur during critical flight phases, such as take-off and landing, due to their proximity to ground obstacles.

1.1   Related Works

To address the aforementioned shortcomings of the two-step approach, prior works introduced Direct Position Estimation (DPE) [13–15] to eliminate the need for intermediate range measurements. Instead, DPE uses the maximum likelihood estimation (MLE) to directly estimate navigation solutions in the PVT domain [13, 16]. DPE facilitates a deep coupling of the signals from different satellites, increases the effective signal power [14, 15], and utilizes weak signals that would have otherwise been discarded [7, 17].

Existing works have identified the improved accuracy of DPE in degraded signal environments, using the Cramér-Rao lower bound [18] to prove the higher achievable accuracy of DPE when compared with the two-step ap-
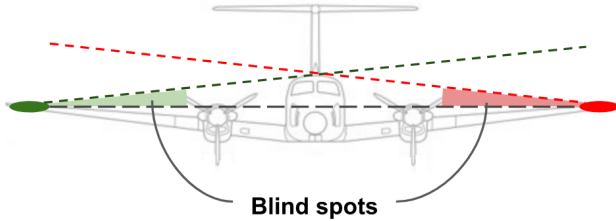
1

Figure 1.1: Visualization of geometric diversity. Two GPS antennas, marked by the solid ovals, are mounted on the wingtips of a fixed-wing aircraft. Both of them have blind spots caused by the fuselage. Fusing their measurements helps create a complete observation of signals from all directions.

proach. Software simulations under various propagation models have also indicated an improved accuracy performance of DPE in noisy signal environments [19–23]. These improvements have been corroborated through live-data experiments, including stationary ground stations [15, 24], a hand-held device near a residential structure [25] and receivers mounted on automobiles [26].

In addition to DPE, multi-receiver architectures have also been discussed [27–29] as means to improve GPS receiver accuracy by installing multiple receivers and their corresponding antennas on a single, rigid platform to increase effective signal power and *geometric redundancy*, as illustrated in Fig. 1.1. Existing works have experimented such architectures on small unmanned aircraft systems (sUAS) [27] and automobiles [28, 29], respectively using STL and VTL receivers as the *constituent receivers* of their networks.

1.2   Our Approach and Contribution

In this work, we propose *Multi-Receiver Direct Position Estimation* (MR-DPE) to improve the measurement certainty of airborne GPS receivers in degraded signal environments by leveraging the benefits of both DPE and the multi-receiver architecture. MR-DPE uses multiple DPE receivers with known antenna baselines to form a receiver network. MR-DPE fuses the signal measurements from different receivers across the network (*i.e.* their likelihood functions with respect to the PVT domain) to generate a likelihood function for the network. An MLE for the navigation solution of the network

then ensues. To accomplish this fusion process, MR-DPE introduces the following novelties:

1. In existing works that discussed multi-receiver networks [27, 29–32], the SNR of each constituent receiver has not been quantitatively involved in the fusion process. In contrast, MR-DPE estimates the noise level in each constituent receiver using MLE and assigns weights to the measurements of the receiver accordingly. Therefore, a constituent receiver with decreasing SNR, which can be symptomatic of the presence of signal challenges, will have a reduced influence over the estimation of the navigation solution of the MR-DPE network.

2. The orientation (*i.e.* the attitude) of the network is essential for the fusion process as the antenna baselines are determined in the network coordinate frame (*e.g.* the body frame of the platform onto which the MR-DPE network is installed) rather than the global frame in which the GPS signals are measured. Multi-receiver architectures that have thus far been proposed do not consider the attitude of the platform as their operation was constrained to shorter antenna baselines [27, 29], or they have employed schemes that are ill-adapted for aerial environments [28]. Following the principle of DPE, we present a new, MLE-based algorithm that is capable of estimating the orientation of an aerial platform.

3. Existing works have not explored the operation of DPE in aerial environments, which are characterized by a more dynamic motion profile and a more rigorous requirement for receiver performance [33]. In this work, full-scale flight tests were conducted on a fixed-wing aircraft [34] to evaluate the performance of MR-DPE in scenarios where signal multipath and masking were prevalent. For instance, in one of the test points, the aircraft flew in a river valley, below the ridge lines, with the heights of the surrounding terrain exceeding the aircraft altitude by more than 500 meters.

It is also worth noting that none of the aforementioned features has been investigated in depth in our preliminary work on MR-DPE [35].

The remainder of the thesis is organized as follows. Chapter 2 details the operating principles of a standalone DPE receiver, which later becomes

the building block of MR-DPE. Chapter 3 provides the mathematical formulations and algorithmic details of MR-DPE. Chapter 4 describes the implementation and the experimentation setup. The test points evaluated in the experiment, their preliminary results and the corresponding analyses are presented in Chapter 5. Finally, Chapter 6 summarizes the thesis.

CHAPTER 2

BACKGROUND

This chapter provides an overview for the principle of DPE, including both mathematical formulations and practical considerations. Understanding this background is essential as the architecture of a standalone DPE receiver is later adapted into the MR-DPE network for joint operation.

2.1 PVT-Domain Maximum Likelihood Estimation

The goal of DPE is to estimate the PVT coordinate of a receiver $\boldsymbol{X}$ based on its observation of the signal Y, where:

$$\boldsymbol{X} \triangleq \begin{bmatrix} x & y & z & c\delta t & \dot{x} & \dot{y} & \dot{z} & c\dot{\delta t} \end{bmatrix}^{\top} = \begin{bmatrix} \boldsymbol{x} \\ \dot{\boldsymbol{x}} \end{bmatrix} \tag{2.1}$$

Note that $\boldsymbol{x} \triangleq \begin{bmatrix} x & y & z & c\delta t \end{bmatrix}^{\top}$ and $(c\delta t, c\dot{\delta t})$ are the receiver-specific clock bias and drift, multiplied by the speed of light, c.

The signal observation at the instance t and with the carrier frequency $f_{\mathrm{L1}} = 1575.42$ MHz wiped off is modeled as:

$$Y(\boldsymbol{a}, \boldsymbol{X}, t) = \sum_{i=1}^{L} a^{(i)} g^{(i)} \left(t - \tau^{(i)} \right) \exp \left\{ j2\pi \Delta f^{(i)} t \right\} + n(t) \tag{2.2}$$

where

- $L \in \mathbb{N}$ is the number of visible satellites.

- $\boldsymbol{a} = \begin{bmatrix} a^{(1)} & a^{(2)} & \cdots & a^{(L)} \end{bmatrix}^{\top} \in \mathbb{C}^{L}$ are the complex amplitudes of the visible satellites.

- $g^{(i)}$ is the L1 coarse acquisition (C/A) code of the i-th visible satellite.

5

- $\tau^{(i)}$ is the code delay of the i-th visible satellite:

$$\tau(i) = \frac{\|\boldsymbol{r}^{(i)}\|}{c} + (\delta t - \delta t^{(i)}) \tag{2.3}$$

- $\Delta f^{(i)}$ is the carrier Doppler shift of the i-th visible satellite:

$$\Delta f^{(i)} = -\frac{f_{\mathrm{L1}}}{c} \cdot \left[\frac{\boldsymbol{r}^{(i)} \cdot \dot{\boldsymbol{r}}^{(i)}}{\|\boldsymbol{r}^{(i)}\|} + c(\dot{\delta t} - \dot{\delta t}^{(i)}) \right] \tag{2.4}$$

- $\boldsymbol{r}^{(i)} = \begin{bmatrix} x - x^{(i)} & y - y^{(i)} & z - z^{(i)} \end{bmatrix}^{\top}$ is the spatial vector to the i-th visible satellite.

- $(\delta t^{(i)}, \dot{\delta t}^{(i)})$ are the clock bias and clock drift specific to the i-th satellite.

- $n(t) \sim \mathcal{N}(0, \sigma^2) \in \mathbb{C}$ is an independent and identically distributed (i.i.d.) Gaussian process, emulating the complex additive white Gaussian noise (AWGN) [13, 15].

Note that a DPE receiver requires the presence of ephemerides to obtain the PVT coordinate of the i-th visible satellite $\boldsymbol{X}^{(i)}$. In this work, it is assumed, without loss of generality, that the ephemerides have been obtained from an external source.

DPE then proceeds to perform maximum likelihood estimation in the PVT domain [13]

$$p(\boldsymbol{y}|\boldsymbol{a}, \boldsymbol{X}, \sigma^2) = \left(\frac{1}{\sqrt{2\pi\sigma^2}} \right)^N \exp\left\{ -\frac{\|\boldsymbol{y} - D\boldsymbol{a}\|^2}{2\sigma^2} \right\} \tag{2.5}$$

where

- $\boldsymbol{y} = \begin{bmatrix} Y(\boldsymbol{a}, \boldsymbol{X}, t_1) & \cdots & Y(\boldsymbol{a}, \boldsymbol{X}, t_N) \end{bmatrix}^{\top} \in \mathbb{C}^N$ is a signal snapshot obtained over $\boldsymbol{t} = \{t_n\}_{n=1}^{N}$.

- $D = D(\boldsymbol{X}, \boldsymbol{t}) \in \mathbb{C}^{N \times L}$ is a matrix of signal replicas from the visible satellites for a given PVT coordinate $\boldsymbol{X}$ and time frame $\boldsymbol{t}$ and assuming uniform amplitudes:

$$[D(\boldsymbol{X}, \boldsymbol{t})]_{i,j} = g^{(i)}(t_j - \tau^{(i)}) \exp\{j2\pi\Delta f^{(i)} t_j\} \tag{2.6}$$

- $\sigma^2 \in \mathbb{R}$ is the noise level of the receiver.

The ML estimation is then obtained [13, 16]:

$$\hat{\boldsymbol{a}}_{\mathrm{ML}}, \hat{\boldsymbol{X}}_{\mathrm{ML}} = \arg\min_{\boldsymbol{a}, \boldsymbol{X}} \|\boldsymbol{y} - D\boldsymbol{a}\|^2 \tag{2.7}$$

By applying the orthogonality principle to Eq. (2.7) [13], we have:

$$\hat{\boldsymbol{a}}_{\mathrm{ML}} = D^+(\hat{\boldsymbol{X}}_{\mathrm{ML}}, \boldsymbol{t})\boldsymbol{y} \tag{2.8}$$

where

- $D^+ = (D^*D)^{-1}D^*$ is the Moore-Penrose pseudoinverse matrix of D.

- D^* is the Hermitian transpose of D.

Replacing $\boldsymbol{a}$ in Eq. (2.7) with $\hat{\boldsymbol{a}}_{\mathrm{ML}}$ from Eq. (2.8), we have:

$$\hat{\boldsymbol{X}}_{\mathrm{ML}} = \arg\min_{\boldsymbol{X}} \|\boldsymbol{y}\|^2 - \boldsymbol{y}^* D\hat{\boldsymbol{a}}_{\mathrm{ML}} = \arg\max_{\boldsymbol{X}} \boldsymbol{y}^* DD^+ \boldsymbol{y} \tag{2.9}$$

2.2 Enhancements on DPE Efficiency

In order to reduce the number of computationally expensive operations, *e.g.* matrix multiplication and inversion, the following approximation technique is applied to reduce the computational load incurred by Eq. (2.9).

Observe that

$$[D^*D]_{i,j} = \begin{cases} N, & i = j \\ c_{ij} \ll N, & i \neq j \end{cases} \tag{2.10}$$

as the C/A code sequences of two different satellites have low cross-correlation.

Hence, by applying the approximation $D^*D \approx NI_L$, where I_L is the $L \times L$ identity matrix, we have:

$$D^+ = (D^*D)^{-1}D^* \approx \frac{1}{N}D^* \tag{2.11}$$

by which Eq. (2.9) is approximated as:

$$\hat{\boldsymbol{X}}_{\mathrm{ML}} \approx \arg\max_{\boldsymbol{X}} \frac{1}{N}\boldsymbol{y}^* DD^* \boldsymbol{y} = \arg\max_{\boldsymbol{X}} \mathcal{R}(\boldsymbol{X}, \boldsymbol{t}) \tag{2.12}$$

where

$$\mathcal{R}(\boldsymbol{X}, \boldsymbol{t}) \triangleq \|D^*(\boldsymbol{X}, \boldsymbol{t})\boldsymbol{y}\|^2 \tag{2.13}$$

Note that existing works have discussed the technique of data-bit aiding [14, 25] to alleviate the effects of bit transitions on the coherent integration, which the term $D^*(\boldsymbol{X}, \boldsymbol{t})\boldsymbol{y}$ essentially is.

By evaluating $\mathcal{R}$ over a spatial and temporal span, the DPE receiver generates a *correlation manifold*, which in turn reflects the spatial and temporal distribution of the likelihood function. The manifold $\mathcal{R}(\cdot)$ then becomes the measurement of a DPE receiver.

CHAPTER 3

MULTI-RECEIVER DIRECT POSITION ESTIMATION

MR-DPE deploys K DPE receivers as its *constituent receivers* and organizes them into a receiver network. This network aggregates the measurements of the constituent receivers, *i.e.* their respective correlation manifolds $\mathcal{R}_k$, and derives a joint, network-level navigation solution accordingly.

3.1   MR-DPE Overview

One of the key premises of MR-DPE is that the antenna baseline information is readily available to the network. For instance, a rigid platform, such as a fixed wing aircraft, would provide stationary antenna baselines that can be surveyed beforehand and known to the MR-DPE network.

This assumption of known antenna baselines facilitates the coupling of the PVT coordinates of the constituent receivers via linear transformations, to wit:

$$\boldsymbol{X}_k = \boldsymbol{X}_o + \overset{\leftrightarrow}{R}(\boldsymbol{X}_o, \boldsymbol{\phi})\boldsymbol{b}_k \tag{3.1}$$

where

- $\boldsymbol{X}_k \in \mathbb{R}^8$ is the PVT coordinate of the k-th constituent receiver.

- $\boldsymbol{X}_o \in \mathbb{R}^8$ is the PVT coordinate of a predetermined reference point O for the network (*e.g.* the network centroid).

- $\boldsymbol{b}_k \in \mathbb{R}^3$ is the antenna baseline of the k-th constituent receiver with respect to O, as defined in the local frame ("ℓ"-frame) of the network (*e.g.* the body frame of the platform on which the MR-DPE network is installed).

- $\boldsymbol{\phi} \in \mathbb{R}^6$ is the Euler angles (yaw, pitch, roll) and its first derivative (*i.e.* the angular rate) of the network with respect to the local tangent plane

(*i.e.* the East-North-Up plane, ENU):

$$\boldsymbol{\phi} = \begin{bmatrix} \alpha & \beta & \gamma & \dot{\alpha} & \dot{\beta} & \dot{\gamma} \end{bmatrix}^\top = \begin{bmatrix} \boldsymbol{\alpha} \\ \dot{\boldsymbol{\alpha}} \end{bmatrix} \tag{3.2}$$

- $\overset{\leftrightarrow}{R} = \overset{\leftrightarrow}{R}(\boldsymbol{X}_o, \boldsymbol{\phi}) \in \mathbb{R}^{8 \times 3}$ is the baseline projection matrix that rotates the ℓ-frame such that its axes are aligned with the global Earth-Centered Earth-Fixed (ECEF) coordinate frame:

$$\overset{\leftrightarrow}{R} = \begin{bmatrix} \overset{\leftrightarrow}{R}_{\text{ECEF/ENU}} \overset{\leftrightarrow}{R}_{\text{ENU}/\ell} \\ \mathbf{0}_{1 \times 3} \\ \overset{\leftrightarrow}{R}_{\text{ECEF/ENU}} [\dot{\boldsymbol{\alpha}}]_\times \overset{\leftrightarrow}{R}_{\text{ENU}/\ell} \\ \mathbf{0}_{1 \times 3} \end{bmatrix} \tag{3.3}$$

- $\overset{\leftrightarrow}{R}_{\text{ECEF/ENU}} = \overset{\leftrightarrow}{R}_{\text{ECEF/ENU}}(\boldsymbol{X}_o) \in \mathbb{R}^{3 \times 3}$ aligns an ENU frame with respect to O with the ECEF frame:

$$\overset{\leftrightarrow}{R}_{\text{ECEF/ENU}} = \overset{\leftrightarrow}{R}_3 \left(-\text{Lon}(\boldsymbol{X}_o) - \frac{\pi}{2} \right) \overset{\leftrightarrow}{R}_1 \left(\text{Lat}(\boldsymbol{X}_o) - \frac{\pi}{2} \right) \tag{3.4}$$

where $\text{Lat}(\cdot)$ and $\text{Lon}(\cdot)$ are respectively the latitude and the longitude of a given global coordinate.

- $\overset{\leftrightarrow}{R}_1(\theta), \overset{\leftrightarrow}{R}_2(\theta), \overset{\leftrightarrow}{R}_3(\theta) \in \mathbb{R}^{3 \times 3}$ are the rotation matrices respectively defined on the principal axes of x, y and z for a given angle θ:

$$\overset{\leftrightarrow}{R}_1(\theta) = \begin{bmatrix} 1 & 0 & 0 \\ 0 & \cos\theta & -\sin\theta \\ 0 & \sin\theta & \cos\theta \end{bmatrix}$$

$$\overset{\leftrightarrow}{R}_2(\theta) = \begin{bmatrix} \cos\theta & 0 & \sin\theta \\ 0 & 1 & 0 \\ -\sin\theta & 0 & \cos\theta \end{bmatrix}$$

$$\overset{\leftrightarrow}{R}_3(\theta) = \begin{bmatrix} \cos\theta & -\sin\theta & 0 \\ \sin\theta & \cos\theta & 0 \\ 0 & 0 & 1 \end{bmatrix}$$

- $\overset{\leftrightarrow}{R}_{\text{ENU}/\ell} = \overset{\leftrightarrow}{R}_{\text{ENU}/\ell}(\boldsymbol{\phi}) \in \mathbb{R}^{3 \times 3}$ converts a candidate in the ℓ-frame into

the ENU frame:

$$\overset{\leftrightarrow}{R}_{\text{ENU}/\ell} = \overset{\leftrightarrow}{R}_2(\gamma)\overset{\leftrightarrow}{R}_1(\beta)\overset{\leftrightarrow}{R}_3(\alpha) \tag{3.5}$$

- $[\dot{\boldsymbol{\alpha}}]_{\times} \in \mathbb{R}^{3\times 3}$ is a skew-symmetric matrix of $\dot{\boldsymbol{\alpha}}$ such that

$$[\dot{\boldsymbol{\alpha}}]_{\times} \boldsymbol{v} = [\dot{\boldsymbol{\alpha}}] \times \boldsymbol{v} \quad \forall \dot{\boldsymbol{\alpha}} \in \mathbb{R}^3$$

Note that it is assumed in this work, without loss of generality, that the constituent receivers are driven by a common clock.

3.1.1   Maximum Likelihood Estimation

As in Chapter 2, the noise in all constituent receivers is assumed to be AWGN. The conditional distribution of a signal snapshot $\boldsymbol{y}_k$ taken over $\boldsymbol{t}$ at the k-th receiver is therefore:

$$p(\boldsymbol{y}_k|\boldsymbol{a}_k, \boldsymbol{X}_o, \boldsymbol{\phi}, \sigma_k^2) = \left(\frac{1}{\sqrt{2\pi\sigma_k^2}}\right)^N \exp\left\{-\frac{\|\boldsymbol{y}_k - D_k\boldsymbol{a}_k\|^2}{2\sigma_k^2}\right\} \tag{3.6}$$

where

$$D_k(\boldsymbol{X}_o, \boldsymbol{\phi}, \boldsymbol{t}) = D\left(\boldsymbol{X}_o + \overset{\leftrightarrow}{R}(\boldsymbol{X}_o, \boldsymbol{\phi})\boldsymbol{b}_k, \boldsymbol{t}\right) = D(\boldsymbol{X}_k, \boldsymbol{t}) \tag{3.7}$$

Following the assumption of independent Gaussian processes for the noise in each constituent receiver, we have:

$$p\left(\{\boldsymbol{y}_k\}_{k=1}^K|\{\boldsymbol{a}_k\}_{k=1}^K, \boldsymbol{X}_o, \boldsymbol{\phi}, \{\sigma_k^2\}_{k=1}^K\right) = \prod_{k=1}^K p(\boldsymbol{y}_k|\boldsymbol{a}_k, \boldsymbol{X}_o, \boldsymbol{\phi}, \sigma_k^2) \tag{3.8}$$

The corresponding log-likelihood function then becomes:

$$\log \mathcal{L}\left(\{\boldsymbol{a}_k\}_{k=1}^K, \boldsymbol{X}_o, \boldsymbol{\phi}, \{\sigma_k^2\}_{k=1}^K\right) = -\sum_{k=1}^K \left(\frac{N}{2}\log(2\pi\sigma_k^2) + \frac{\|\boldsymbol{y}_k - D_k\boldsymbol{a}_k\|^2}{2\sigma_k^2}\right)$$

which leads us to the maximum likelihood estimation:

$$\hat{\boldsymbol{X}}_{o,\text{ML}}, \hat{\boldsymbol{\phi}}_{\text{ML}} = \arg\max_{\boldsymbol{X}_o, \boldsymbol{\phi}} \left(\sum_{k=1}^K \frac{\boldsymbol{y}_k^* D_k \hat{\boldsymbol{a}}_{k,\text{ML}}}{\hat{\sigma}_{k,\text{ML}}^2}\right) \tag{3.9}$$

$$\hat{\sigma}_{k,\text{ML}}^2 = \frac{\|\boldsymbol{y}_k - \hat{D}_{k,\text{ML}}\hat{\boldsymbol{a}}_{k,\text{ML}}\|^2}{N} \tag{3.10}$$

$$\hat{\boldsymbol{a}}_{k,\text{ML}} = \hat{D}_{k,\text{ML}}^{+} \boldsymbol{y}_k \qquad (3.11)$$

where $\hat{D}_{k,\text{ML}} \triangleq D_k(\hat{\boldsymbol{X}}_{o,\text{ML}}, \hat{\boldsymbol{\phi}}_{\text{ML}}, \boldsymbol{t})$ follows the definition in Eq. (3.7) and $D^+ = (D^*D)^{-1}D^*$ is the Moore-Penrose pseudoinverse matrix of D.

Equation (3.9) highlights the ability of MR-DPE to simultaneously optimize the PVT coordinate and the orientation of the network, a capability not found in prior works on multi-receiver architectures [27–29].

3.1.2   Cramér-Rao Lower Bound

Recall that for any distribution of the exponential family (*e.g.* the Gaussian distribution), the maximum-likelihood estimator and the minimum-variance unbiased estimator (MVUE) are identical for a given distribution parameter $\boldsymbol{\theta}$.

The estimators of Eq. (3.9), Eq. (3.10) and Eq. (3.11) are therefore MVUE estimators to the parameter set $\boldsymbol{\theta}_o = \left\{ \{\boldsymbol{a}_k\}_{k=1}^{K}, \boldsymbol{X}_o, \boldsymbol{\phi}, \{\sigma_k^2\}_{k=1}^{K} \right\}$, and their covariance is bounded by the Cramér-Rao lower bound:

$$\text{Cov}[\hat{\boldsymbol{\theta}}_o | \boldsymbol{\theta}_o] \preceq I_{\boldsymbol{\theta}_o}^{-1}$$

where $I_{\boldsymbol{\theta}_o} \triangleq \mathbb{E}\left[-\nabla_{\boldsymbol{\theta}_o}^2 \log p\left(\{\boldsymbol{y}_k\}_{k=1}^{K} | \boldsymbol{\theta}_o \right) \right]$ is the Fisher Information matrix of $\boldsymbol{\theta}_o$.

From Eq. (3.8), it is then derived that:

$$I_{\boldsymbol{\theta}_o} = \mathbb{E}[-\nabla_{\boldsymbol{\theta}_o}^2 \log \prod_{k=1}^{K} p\left(\boldsymbol{y}_k | \boldsymbol{\theta}_k\right)] = \sum_{k=1}^{K} \mathbb{E}[-\nabla_{\boldsymbol{\theta}_o}^2 \log p\left(\boldsymbol{y}_k | \boldsymbol{\theta}_k\right)] = \sum_{k=1}^{K} I_{\boldsymbol{\theta}_o,k}$$

$$(3.12)$$

where $\boldsymbol{\theta}_k = \{\boldsymbol{a}_k, \boldsymbol{X}_o, \boldsymbol{\phi}, \sigma_k^2\}$.

That is, an increasing number of constituent receivers in the MR-DPE network will result in a corresponding lowering of the Cramér-Rao bound and, therefore, an improvement on the attainable accuracy.

3.1.3   Efficiency Considerations

The efficiency of the generic, analytic DPE algorithm described in Sec. 2.1 is impeded by two major factors:

1. its computationally expensive operations, *e.g.* matrix multiplication and inversion, and

2. its nature as a high-dimensional optimization problem [23, 36, 37].

As these challenges are inherited by MR-DPE, the following techniques are deployed to avoid the prohibitive computational cost:

- The term $\boldsymbol{y}^* D_k \boldsymbol{a}_k$, found in Eq. (3.9) and Eq. (3.10), is replaced with $\frac{1}{N}\|D_k^* \boldsymbol{y}\|^2$ per Eq. (2.11). We hence derive from Eq. (2.13), Eq. (3.7) and Eq. (3.9):

$$\mathcal{R}_k(\boldsymbol{X}_o, \boldsymbol{\phi}, \boldsymbol{t}) = \|D_k^*(\boldsymbol{X}_o, \boldsymbol{\phi}, \boldsymbol{t})\boldsymbol{y}_k\|^2 \tag{3.13}$$

$$\mathcal{R}_o\left(\boldsymbol{X}_o, \boldsymbol{\phi}, \{\sigma_k^2\}, \boldsymbol{t}\right) = \sum_{k=1}^{K} \frac{\mathcal{R}_k(\boldsymbol{X}_o, \boldsymbol{\phi}, \boldsymbol{t})}{\sigma_k^2} \tag{3.14}$$

which are the correlation manifold of the k-th constituent receiver and the correlation manifold of the network, respectively.

Applying the same approximation to Eq. (3.10), the noise level in the k-th constituent receiver is approximated as:

$$\hat{\sigma}_{k,\mathrm{MR}}^2 = \frac{\|\boldsymbol{y}_k\|^2 - \frac{1}{N}\mathcal{R}_k(\hat{\boldsymbol{X}}_{o,\mathrm{MR}}, \hat{\boldsymbol{\phi}}_{\mathrm{MR}}, \boldsymbol{t})}{N} \tag{3.15}$$

- The high-dimensional search space for $\{\boldsymbol{X}_o, \boldsymbol{\phi}\}$ is decoupled into multiple subspaces, similar to the Space-Alternating Generalized Expectation (SAGE) algorithms discussed in [23, 36, 37]. These subspaces are:

    - Network position/clock bias $\boldsymbol{x}_o$.
    - Network velocity/clock drift $\dot{\boldsymbol{x}}_o$.
    - Network attitude $\boldsymbol{\alpha}$.
    - Network angular rate $\dot{\boldsymbol{\alpha}}$.

The decoupling process requires some filtering techniques to provide reasonable predictions for the PVT coordinate and the orientation of the platform, while what constitutes reasonable depends on the application [23]:

13

$$\bar{\boldsymbol{X}}_o(\boldsymbol{t}) = F_{\boldsymbol{X}}\hat{\boldsymbol{X}}_o(\boldsymbol{t} - \Delta T) = \begin{bmatrix} \bar{\boldsymbol{x}}_o \\ \bar{\dot{\boldsymbol{x}}}_o \end{bmatrix} \tag{3.16}$$

$$\bar{\boldsymbol{\phi}}(\boldsymbol{t}) = F_{\boldsymbol{\phi}}\hat{\boldsymbol{\phi}}(\boldsymbol{t} - \Delta T) = \begin{bmatrix} \bar{\boldsymbol{\alpha}} \\ \bar{\dot{\boldsymbol{\alpha}}} \end{bmatrix} \tag{3.17}$$

where $F_{\boldsymbol{X}} \in \mathbb{R}^{8\times 8}$ and $F_{\boldsymbol{\phi}} \in \mathbb{R}^{6\times 6}$ are prediction matrices provided by the chosen filtering technique. For the scope of this work, we have found that simple identity matrices suffice our purposes; that is:

$$F_{\boldsymbol{X}} = I_8$$
$$F_{\boldsymbol{\phi}} = I_6$$

Sections 3.2 and 3.3 detail the network PVT and orientation estimations outlined above.

3.2 Estimating Network PVT Coordinate

Figure 3.1 depicts the iterative procedure of estimating the PVT coordinate of the MR-DPE network. For the purpose of clarity, the step-wise insets (i)-(iv) use an example where four color-coded antennas are positioned on the wing tips (left-red, right-green), the nose (orange) and the tail (blue) of a fixed-wing aircraft, and the centroid O is defined at the center of the fuselage. The candidate grids depicted are only in the position domain (x, y, z) for a more intuitive visualization.

An iterative algorithm is devised to estimate the PVT solution of the network and shown in Fig. 3.1. Each iteration consists of the following steps:

1. An iteration begins with the population of the zero-th and the first-order candidate grids, $\{\tilde{\boldsymbol{x}}_{o,p}\}$ and $\{\tilde{\dot{\boldsymbol{x}}}_{o,v}\}$, where

   - $\tilde{\boldsymbol{x}}_{o,p} = \begin{bmatrix} \tilde{x}_{o,p} & \tilde{y}_{o,p} & \tilde{z}_{o,p} & c\tilde{\delta t}_{o,p} \end{bmatrix}^{\top}$ is the p-th candidate for the network position/clock bias.
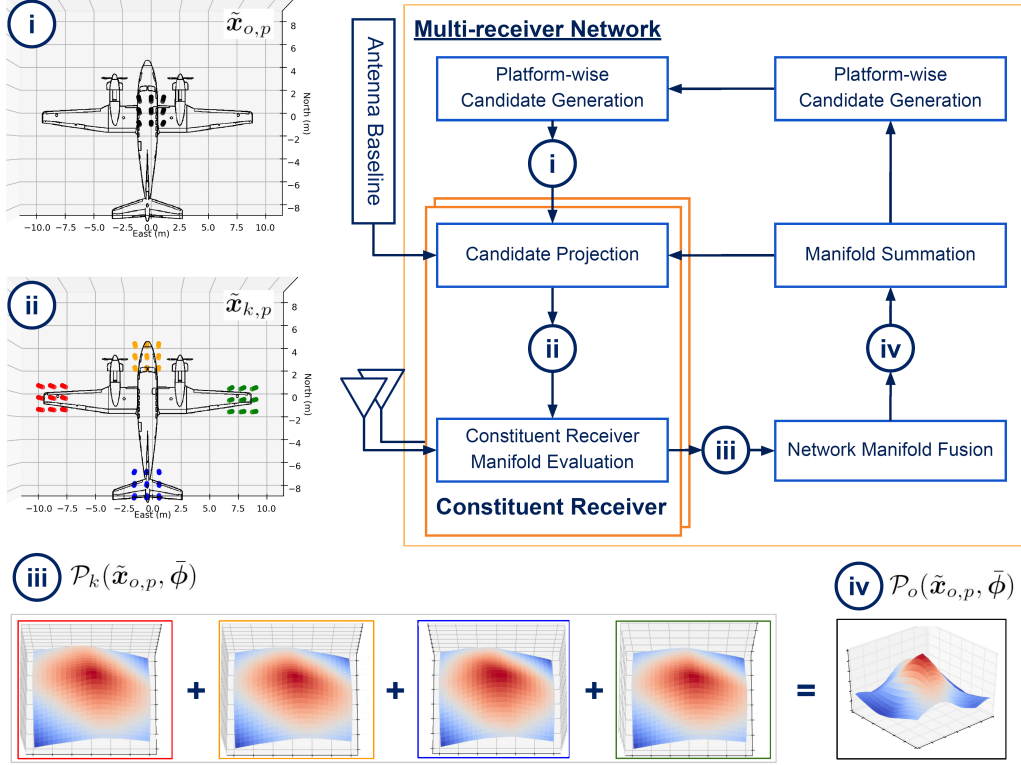
14

Figure 3.1: Block diagram for MR-DPE PVT estimation

- $\tilde{\dot{\boldsymbol{x}}}_{o,v} = \begin{bmatrix} \tilde{\dot{x}}_{o,v} & \tilde{\dot{y}}_{o,v} & \tilde{\dot{z}}_{o,v} & c\tilde{\dot{\delta t}}_{o,v} \end{bmatrix}^{\top}$ is the v-th candidate for the network velocity/clock drift.

This is shown in Fig. 3.1 as step (i), in which the network candidates are depicted as black discs surrounding the center of the fuselage. Each candidate is unique and represents a potential solution in its corresponding subspace [14, 23, 24]. MR-DPE then seeks the candidates that maximize Eq. (3.14). This numerical approach is preferred over an analytic approach as Eq. (3.9) lacks closed-form solutions [13–15].

2. By the relationship established in Eq. (3.1), the candidate grids $\{\tilde{\boldsymbol{x}}_{o,p}\}, \{\tilde{\dot{\boldsymbol{x}}}_{o,v}\}$ are projected to the mounting points of the antennas of the constituent receivers. This creates K candidate grids for both the zeroth-order and the first-order terms:

$$\begin{bmatrix} \tilde{\boldsymbol{x}}_{k,p} \\ \tilde{\dot{\boldsymbol{x}}}_{k,v} \end{bmatrix} = \begin{bmatrix} \tilde{\boldsymbol{x}}_{o,p} \\ \tilde{\dot{\boldsymbol{x}}}_{o,v} \end{bmatrix} + \overset{\leftrightarrow}{R}(\bar{\boldsymbol{X}}_o, \bar{\boldsymbol{\phi}})\boldsymbol{b} \qquad (3.18)$$

Note that Eq. (3.18) does not imply dependence between the p-th zeroth-order candidate and the v-th first-order candidate.

This step is depicted in Fig. 3.1 as step (ii). The corresponding inset shows that the black candidate grid near the center of the fuselage is now replaced by the four color-coded grids, each surrounding one of the antenna mounting points.

3. Following the projection of the candidate grids, each constituent receiver evaluates two correlation manifolds, one for the position/clock bias candidates:

$$\mathcal{P}_k(\tilde{\boldsymbol{x}}_{o,p}, \bar{\boldsymbol{\phi}}, \boldsymbol{t}) \triangleq \mathcal{R}_k\left(\begin{bmatrix} \tilde{\boldsymbol{x}}_{o,p} \\ \bar{\tilde{\boldsymbol{x}}}_o \end{bmatrix}, \bar{\boldsymbol{\phi}}, \boldsymbol{t} \right) \tag{3.19}$$

and one for the velocity/clock drift candidates:

$$\mathcal{V}_k(\tilde{\boldsymbol{x}}_{o,v}, \bar{\boldsymbol{\phi}}, \boldsymbol{t}) \triangleq \mathcal{R}_k\left(\begin{bmatrix} \bar{\boldsymbol{x}}_o \\ \tilde{\boldsymbol{x}}_{o,v} \end{bmatrix}, \bar{\boldsymbol{\phi}}, \boldsymbol{t} \right) \tag{3.20}$$

where $\mathcal{R}_k$ is defined in Eq. (3.13).

Step (iii) in Fig. 3.1 provides visualization for the evaluation of these receiver-level correlation manifolds.

4. The MR-DPE network then aggregates the receiver-level manifolds based on Eq. (3.14), as shown in step (iv) of Fig. 3.1.

The resulting manifolds are the network position/clock bias manifold $\mathcal{P}_o$ and the network velocity/clock drift manifold $\mathcal{V}_o$:

$$\mathcal{P}_o(\tilde{\boldsymbol{x}}_{o,p}, \bar{\boldsymbol{\phi}}, \boldsymbol{t}) \triangleq \mathcal{R}_o\left(\begin{bmatrix} \tilde{\boldsymbol{x}}_{o,p} \\ \bar{\tilde{\boldsymbol{x}}}_o \end{bmatrix}, \bar{\boldsymbol{\phi}}, \{\bar{\sigma}_k^2\}, \boldsymbol{t} \right)$$

$$= \sum_{k=1}^{K} \frac{\mathcal{P}_k(\tilde{\boldsymbol{x}}_{o,p}, \bar{\boldsymbol{\phi}}, \boldsymbol{t})}{\bar{\sigma}_k^2} \tag{3.21}$$

$$\mathcal{V}_o(\tilde{\boldsymbol{x}}_{o,v}, \bar{\boldsymbol{\phi}}, \boldsymbol{t}) \triangleq \mathcal{R}_o\left(\begin{bmatrix} \bar{\boldsymbol{x}}_o \\ \tilde{\boldsymbol{x}}_{o,v} \end{bmatrix}, \bar{\boldsymbol{\phi}}, \{\bar{\sigma}_k^2\}, \boldsymbol{t} \right)$$

$$= \sum_{k=1}^{K} \frac{\mathcal{V}_k(\tilde{\boldsymbol{x}}_{o,v}, \bar{\boldsymbol{\phi}}, \boldsymbol{t})}{\bar{\sigma}_k^2} \tag{3.22}$$

16

where $\bar{\sigma}_k^2(\boldsymbol{t}) \triangleq \hat{\sigma}_{k,\mathrm{MR}}^2(\boldsymbol{t} - \Delta T)$, with the RHS term defined in Eq. (3.15). That is, we approximate the noise level in each constituent receiver as constant given any two consecutive signal snapshots, $\boldsymbol{y}_k(\boldsymbol{t} - \Delta T)$ and $\boldsymbol{y}_k(\boldsymbol{t})$.

5. Lastly, the PVT solution, $\hat{\boldsymbol{X}}_{o,\mathrm{MR}}$, is determined using maximum-likelihood estimation, namely:

$$\hat{\boldsymbol{X}}_{o,\mathrm{MR}} = \begin{bmatrix} \arg\max_{\tilde{\boldsymbol{x}}_{o,p}} \mathcal{P}_o(\tilde{\boldsymbol{x}}_{o,p}, \bar{\phi}, \boldsymbol{t}) \\ \arg\max_{\tilde{\boldsymbol{x}}_{o,v}} \mathcal{V}_o(\tilde{\boldsymbol{x}}_{o,v}, \bar{\phi}, \boldsymbol{t}) \end{bmatrix} \tag{3.23}$$

Careful readers will note from Eq. (3.21) and Eq. (3.22) that the noise level σ_k^2 of each constituent receiver is integrated into the fusion of the correlation manifolds. That is, the higher the noise level is in one receiver, the less the receiver contributes to the estimation of the network PVT solution $\hat{\boldsymbol{X}}_{\mathrm{MR}}$. Therefore, the fusion process not only utilizes the information redundancy gained by the additional signal observation, but intelligently considers the quality of the signal from each receiver before its measurements are fused into the network. This approach is particularly important for scenarios when signal challenges are limited to certain constituent receivers within the network. In this case, the network is able to reduce the influence of these affected receivers on its navigation solution.

Last but not least, it is worth noting that the algorithm presented in this section requires the presence of the attitude information $\boldsymbol{\phi}$ to complete the estimation for the PVT coordinate of the network. Therefore, during each complete iteration of MR-DPE execution, the PVT estimation algorithm and the attitude estimation algorithm that is to be presented in Sec. 3.3 proceed sequentially to supply essential information to each other.

3.3 Estimating Network Orientation

Similar to the PVT estimation algorithm introduced in Sec. 3.2, the orientation estimation algorithm for MR-DPE executes iteratively using a grid of *orientation* candidates, each representing a unique combination of angles and angular velocities.

1. First, two three-dimensional orientation candidate grids, $\{\tilde{\boldsymbol{\alpha}}_u\}$ and $\{\tilde{\boldsymbol{\alpha}}_w\}$, are populated, where

   - $\{\tilde{\boldsymbol{\alpha}}_u\} = \begin{bmatrix} \tilde{\alpha}_u & \tilde{\beta}_u & \tilde{\gamma}_u \end{bmatrix}^T$ is the u-th attitude candidate.

   - $\tilde{\dot{\boldsymbol{\alpha}}}_w = \begin{bmatrix} \tilde{\dot{\alpha}}_u & \tilde{\dot{\beta}}_u & \tilde{\dot{\gamma}}_u \end{bmatrix}^T$ is the w-th angular-rate candidate.

   These two grids are centered at an initializing value, which may be obtained from various sources, *e.g.* the prediction $\bar{\boldsymbol{\phi}}_o$ based on the previous iteration.

2. Two correlation manifolds, $\mathcal{U}$ and $\mathcal{W}$, are then evaluated, in a fashion similar to Eq. (3.21) and Eq. (3.22), to wit:

$$\mathcal{U}(\tilde{\boldsymbol{\alpha}}_u, \boldsymbol{t}) \triangleq \mathcal{R}_o\left(\bar{\boldsymbol{X}}_o, \begin{bmatrix} \tilde{\boldsymbol{\alpha}}_u \\ \bar{\dot{\boldsymbol{\alpha}}} \end{bmatrix}, \{\bar{\sigma}_k^2\}, \boldsymbol{t}\right) \tag{3.24}$$

$$\mathcal{W}(\tilde{\dot{\boldsymbol{\alpha}}}_w, \boldsymbol{t}) \triangleq \mathcal{R}_o\left(\bar{\boldsymbol{X}}_o, \begin{bmatrix} \bar{\boldsymbol{\alpha}} \\ \tilde{\dot{\boldsymbol{\alpha}}}_w \end{bmatrix}, \{\bar{\sigma}_k^2\}, \boldsymbol{t}\right) \tag{3.25}$$

   That is, instead of projecting a PVT candidate grid to the antenna mounting points with the same network orientation as in Eq. (3.18), a single PVT coordinate is projected with different orientation values, and the correlation values resulting from these different projections are subsequently assessed.

3. Lastly, the candidates that respectively yield the highest $\mathcal{U}$ and $\mathcal{W}$ values are selected as the estimate for the network orientation, namely:

$$\hat{\boldsymbol{\phi}}_{\mathrm{MR}} = \begin{bmatrix} \arg\max_{\tilde{\boldsymbol{\alpha}}_u} \mathcal{U}(\tilde{\boldsymbol{\alpha}}_u, \boldsymbol{t}) \\ \arg\max_{\tilde{\dot{\boldsymbol{\alpha}}}_w} \mathcal{W}(\tilde{\dot{\boldsymbol{\alpha}}}_w, \boldsymbol{t}) \end{bmatrix} \tag{3.26}$$

To better understand the functioning of the orientation estimation algorithm, Fig. 3.2 provides a visualization for Eq. (3.24) using three orientation candidates with different yaw values $\tilde{\alpha}_u$. When the values provided to the orientation candidate diverge from the true orientation of the network, as in the cases on the left and on the right of Fig. 3.2, the position of the propagated candidate drifts off the true position of the antenna. The correlation $\mathcal{U}$ from Eq. (3.24) will thus decrease accordingly.
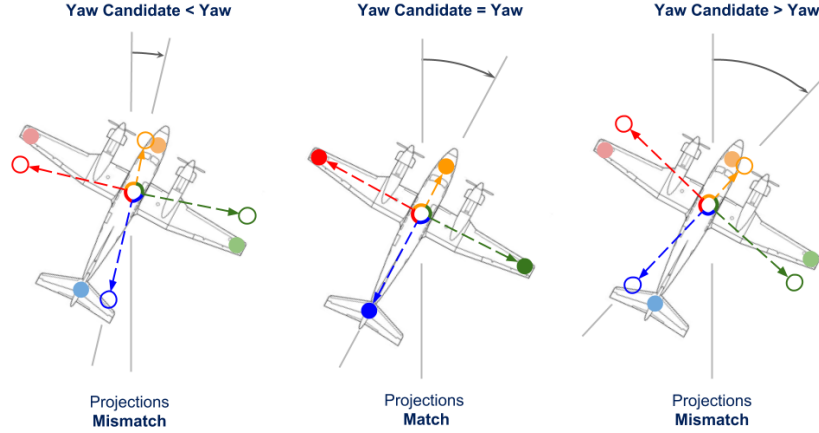
Figure 3.2: A mismatch between an orientation candidate and the true network orientation will result in the decrease of correlation $\mathcal{U}$.
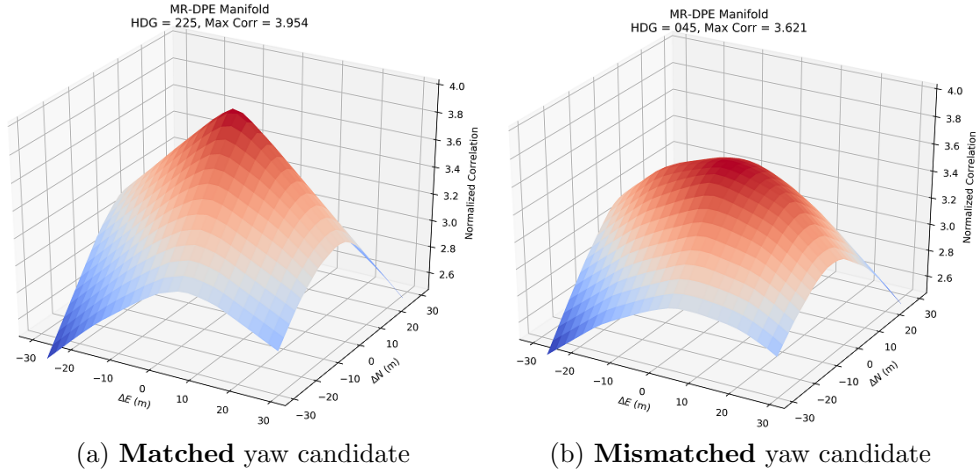

(a) **Matched** yaw candidate

(b) **Mismatched** yaw candidate

Figure 3.3: Attitude correlation manifolds $\mathcal{U}$ with different yaw values $\tilde{\alpha}_u$

Figure 3.3 uses real-world data to support this claim. The heading of the network was at $225°$, and Fig. 3.3(a) depicts the case when the correct orientation value is applied when computing $\mathcal{U}$. Higher correlation values along with a sharper manifold peak are observed when compared with Fig. 3.3(b), where the orientation candidate is set with the heading of $45°$. This results in much lower correlation values and a rounded appearance of the correlation manifold.

CHAPTER 4

IMPLEMENTATION AND EXPERIMENT SETUP

The MR-DPE algorithm introduced in Sec. 3.2 and Sec. 3.3 is implemented with our Python-based software-defined radio (SDR) research suite, `pyGNSS` [28, 38]. The length of each sample block is set at $\Delta T = 20 \times 10^{-3}$ seconds.

4.1 Candidate Grid Configuration

The configuration of the candidate grid is presented in Table 4.1. The pattern of the base grid, which is referred to in Table 4.1, is depicted in Fig. 4.1. The coordinate of the candidates represents its offset from $\{\bar{\boldsymbol{X}}_o, \bar{\boldsymbol{\phi}}\}$ on the specified dimension.

4.2 Hardware Setup

Our experiment platform was a twin-engine, fixed-wing aircraft. Four GPS L1 active antennas were installed onto the aircraft, with one at each wingtip, one in front of the cockpit canopy and one on top of the vertical stabilizer, as shown in Fig. 4.2.

Table 4.1: Candidate Grid Configuration

Domain	Axis	Span	Spacing	#/dim. [a]
Position	East, North, Up	Base grid [b] ×2		21
Velocity	East, North, Up	Base grid ÷10		21
Time	Clock Bias δt	± 125 ns	$\frac{125}{3}$ ns	7
Time	Clock Drift $\dot{\delta t}$	2.5 ns/s	$\frac{5}{6}$ ns/s	7
Orientation	Attitude $\boldsymbol{\alpha}$	$\pm 15°$	$7.5°$	5
Orientation	Angular Rate $\dot{\boldsymbol{\alpha}}$	$\pm 15°/s$	$7.5°/s$	5

[a] Number of candidates per dimension
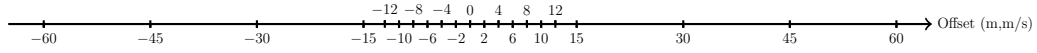[b] The pattern of the base grid is depicted in Fig. 4.1

Figure 4.1: Pattern of the base candidate grid, facilitating the placement of position and velocity candidates

Figure 4.2: Clockwise from top left: flight test aircraft, C-12C Huron; nose antenna (in front of cockpit canopy); tail antenna (on top of vertical stabilizer, not visible) and the measuring of antenna baselines using FARO® FaroArm portable coordinate measuring machine (PCMM); left-wing antenna.

Each antenna is connected to an Ettus Research ^{TM} Universal Software-Radio Peripheral (USRP), a commercial off-the-shelf radio front-end, which records the raw RF samples. The USRPs were operated at the sampling rate of $f_s = 2.5$ MHz and the 3 dB analog bandwidth of 8 MHz. A single SA.45s chip-scale atomic clock (CSAC) provided a 10 MHz $\pm 5 \times 10^{-10}$ Hz clocking signal [39] to all USRP units to ensure low clock-originated errors. The synchronization of the USRP units was achieved via the one-pulse-per-second (1-PPS) signal, which was generated by the CSAC and distributed with the SMA switch. The maximum offset across the USRP units was recorded to be 0.4 μs.

In addition, the aircraft was equipped with a Time-Space Positioning Information (TSPI) system [34, 40], which deployed a kinematic, differential GPS receiver and a tactical-grade IMU [34, 41, 42] to achieve an accuracy of ± 1.5 feet in position, ± 0.02 feet-per-second in velocity, and $0.1°$ in attitude. The TSPI system therefore serves as the truth source for the position, velocity and orientation of the aircraft during the experiments. Figure 4.3 shows the four USRPs and the TSPI system mounted in the flight test aircraft.

Figure 4.3: Equipment rack (bright orange) as installed on board the flight test aircraft. Four USRPs are immediately visible in the bottom-left corner. CSAC is hidden from plain view. The TSPI system (white, orange) is mounted on the floor directly behind the co-pilot's seat.

We also implemented the single-receiver DPE (SR-DPE) algorithm intro-

duced in [26] to serve as the baseline method against which the performance of MR-DPE is evaluated. We elected [26] as it was the only DPE-related work to have performed live-data experiments on a mobile platform. Other previous works on DPE, in contrast, primarily focused on simulations or stationary ground experiments [13–15, 19, 24, 25]. SR-DPE was fed with the data samples collected with the tail antenna, whose elevated mounting point ensured minimal fuselage-induced signal masking.

CHAPTER 5

TEST POINTS AND RESULTS

Based on the implementation and experimentation setup introduced in Chapter 4, three test points have been investigated and their flight characteristics are summarized in Table 5.1. Each of these test points is representative of flight profiles that often expose airborne GPS receivers to signal challenges.

Furthermore, qualitative analyses are performed on the correlation manifolds yielded from the SR-DPE and the MR-DPE implementations. Figure 5.1 shows one such example, when the aircraft was engaged in straight-and-level flight. The relative correlation, shown on the z-axis, is defined as the ratio between the correlation at the given instance for the given candidate and the maximum correlation value attained throughout an entire test point, namely:

$$\frac{\mathcal{P}(\tilde{\boldsymbol{x}}_{o,p}, \boldsymbol{t})}{\max_{\tilde{\boldsymbol{x}}_{o,p}, \boldsymbol{t}} \mathcal{P}(\tilde{\boldsymbol{x}}_{o,p}, \boldsymbol{t})}$$

All test points include a 30-second lead-in phase, during which the aircraft was engaged in straight-and-level flight under open-sky environment. Therefore, the maximum correlation is almost certainly achieved during this period of time and serves as a useful performance benchmark. Figure 5.1, indeed, shows the correlation manifolds during this initialization phase, where the relative correlation peaks of both manifolds exceed 0.9. Furthermore, Fig. 5.2 depicts the cross-sections of the correlation manifolds shown in Fig. 5.1. It is worth noting that while the correlation levels between the SR-DPE and the MR-DPE are similar, the MR-DPE generated a sharper manifold than SR-DPE. The sharper peak indicates higher certainty of the measurements made by MR-DPE; should quantitative analyses be performed, more accurate performance can be expected from MR-DPE.

It is worth emphasizing that this maximum correlation is considered separately for the SR-DPE and the MR-DPE implementations, as the correlation manifold of the MR-DPE is the summation of four constituent DPE receivers,

Table 5.1: Selected Flight Test Points

#	Test Point	Airspeed (knots) [*]	Altitude (feet) [*]	Bank Angle
1	Tower Fly-by [a]	200 ± 10	200 ± 100 AGL [d]	$[-30°, 30°]$
2	Bank-to-Bank Maneuver [b]	160 ± 10	10000 ± 2000 PA [e]	$[-60°, 60°]$
3	Sidewinder Transition [a,b,c]	200 ± 10	≥ 500 AGL	$[-60°, 60°]$

[a] Low-level operation (signal multipath was likely)
[b] Dynamic maneuver
[c] High-terrain environment (signal masking was likely)
[d] Above ground level
[e] Pressure altitude
[*] In this table, the aviation convention of using feet to represent altitude and knots to represent (indicated) airspeed is observed.

resulting in considerably higher correlation values.
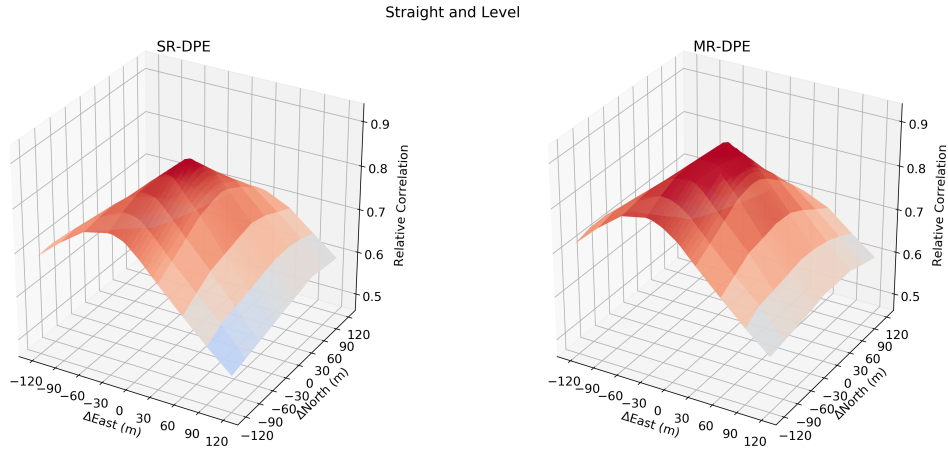
Figure 5.1: Correlation manifolds of SR-DPE and MR-DPE during straight-and-level flight. Note that both implementations achieved high relative correlations.

5.1 Final Approach and Climb-Out

The first test point (tower fly-by) was designed to replicate a signal environment that is commonly encountered during take-off and landing, namely,
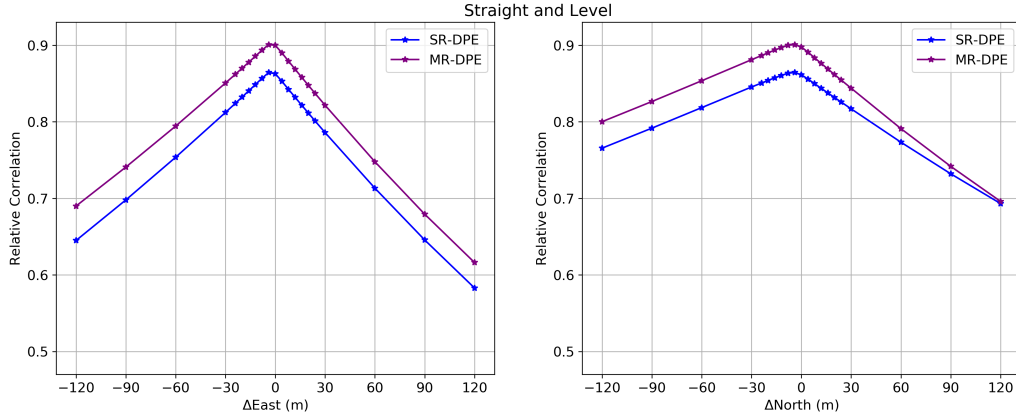
Figure 5.2: Cross-sections of the correlation manifolds during straight-and-level flight, The stars mark the positions where the candidates were placed. While the correlation levels achieved by the SR-DPE and the MR-DPE implementations are similar, the latter generates a notably sharper peak.

when an aircraft is traveling in the proximity of the ground surface and with considerable artificial structures (*e.g.* hangars, towers, terminals) in its surroundings.

During the test point, the aircraft was initially positioned 84 meters above ground level (AGL) and 12 kilometers northeast of the runway. This is depicted in Fig. 5.3. It then gradually descended toward the runway and reached a minimum height of 59 meters AGL, all the while traveling at approximately 108 meters per second. Upon crossing the east end of the runway at $t = 80$, the aircraft initiated a climb-out, with the climb rate varying between 5 and 12.5 meters per second. In Fig. 5.4, the true altitude recorded by the TSPI system is presented alongside the terrain elevation [43] to reflect the relationship between the flight path and the ground surface.

Figure 5.5 depicts the correlation manifold $\mathcal{P}$ at $t = 80$, when the aircraft was transitioning from a shallow descent into a considerably steeper climb. It is readily observed from Fig. 5.5 that a higher relative correlation is achieved using the MR-DPE. This indicates MR-DPE experienced less reduction in its correlation level during the sudden change of flight dynamics when compared with SR-DPE. A higher level of measurement certainty was thus attained through MR-DPE. In addition, Fig. 5.6 presents the cross-sections of the two correlation manifolds respectively generated by the SR-DPE and the MR-DPE implementations. It is worth noting that MR-DPE yielded not
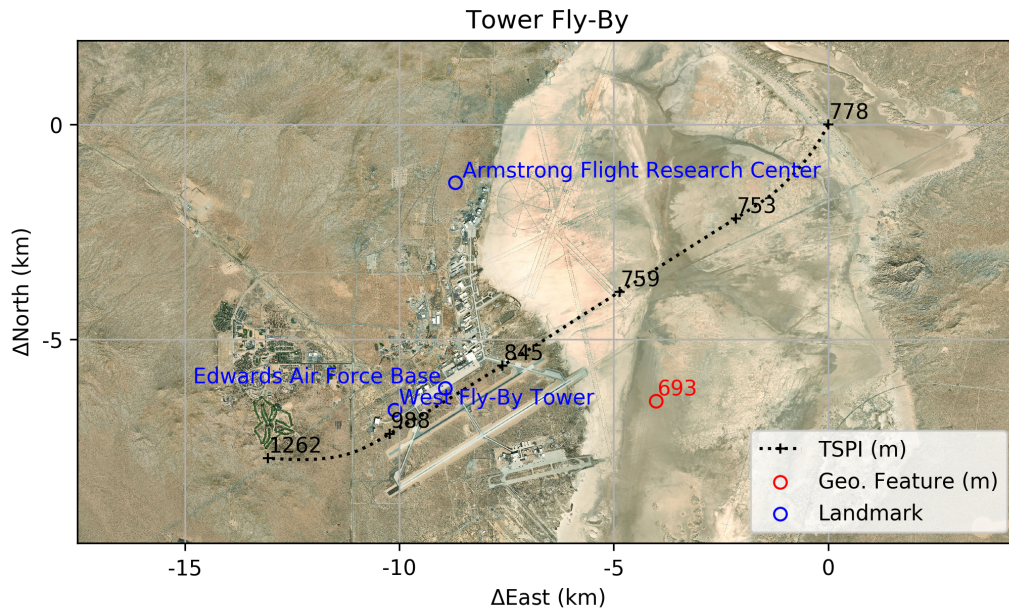
Figure 5.3: Ground track of the tower fly-by (satellite image: [44]). The black markers along the path indicate the altitude of the aircraft at 30-second intervals.
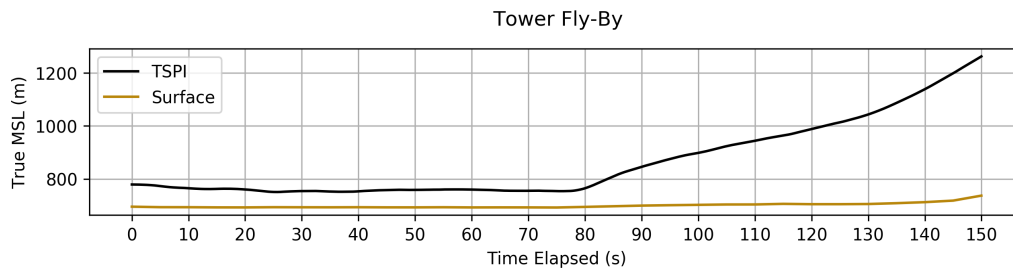

Figure 5.4: The true mean sea level (MSL) altitude as reported by TSPI in black and the elevation of the ground surface in dark gold during the tower fly-by test point

27

only a higher correlation peak, but a manifold that bears a considerably sharper appearance overall.
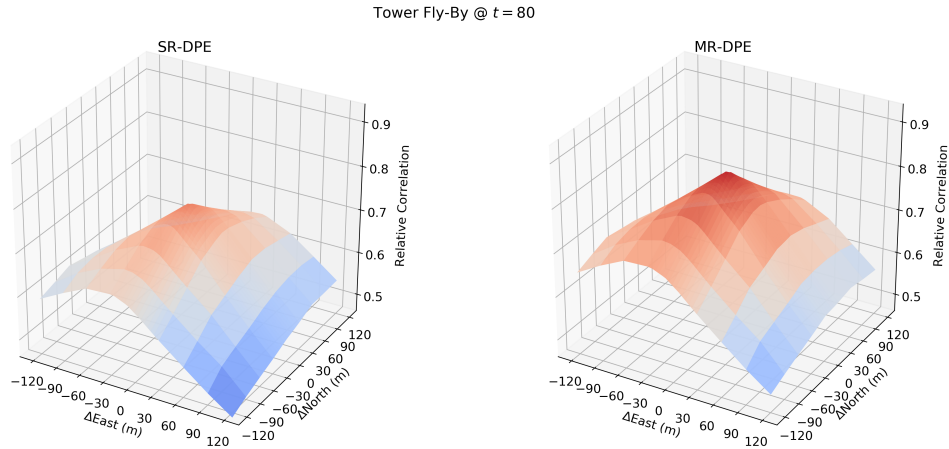

Figure 5.5: Correlation manifolds of SR-DPE and MR-DPE at $t = 80$ during the tower fly-by test point. Note that a higher correlation level is attained using MR-DPE.
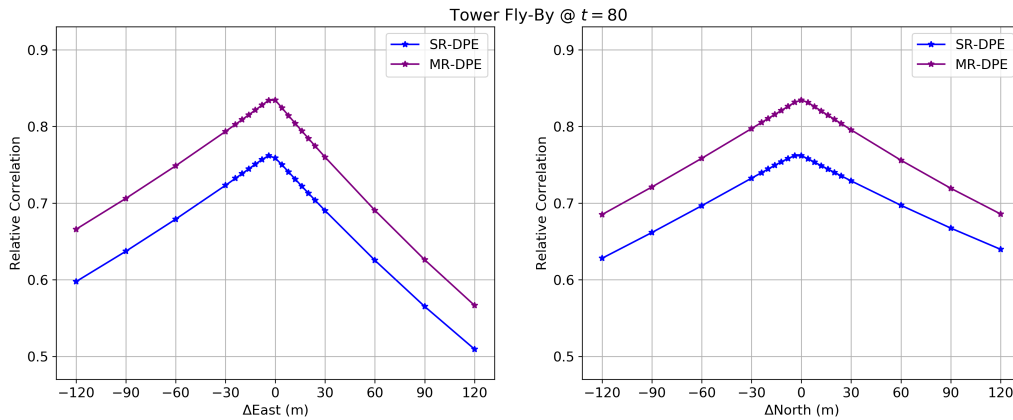
Figure 5.6: Cross-sections of the correlation manifolds at $t = 80$ during the tower fly-by test point. The sharper peak attained by MR-DPE indicates a higher level of measurement certainty.

5.2   Dynamic Maneuvers

In this test point, the aircraft was performing successive, bank-to-bank rolling maneuvers; the ailerons were deflected at three-fourths of their full deflection.

As shown in Fig. 5.7, this resulted in the aircraft swiftly alternating between 60-degree banking to the left $(-)$ and to the right $(+)$. The average time to roll from one side to the other was 5.10 seconds, yielding an average rolling rate of 23.5 degrees per second. Such dynamic maneuvers often result in the loss of track for receivers using the two-step approach due to the constantly changing satellite visibility [35].
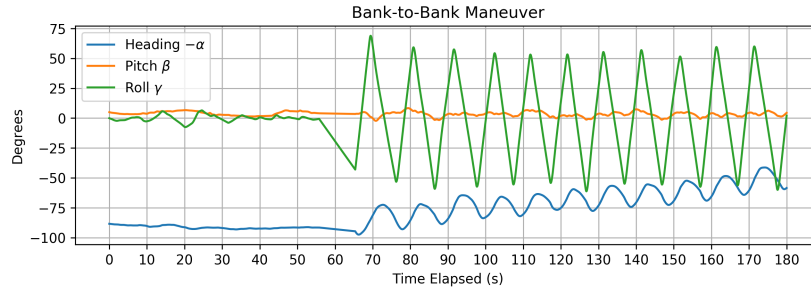

Figure 5.7: Attitude history of the bank-to-bank rolling maneuvers, as recorded by the TSPI system. Other than the swift back-and-forth of the roll angle, the heading of the aircraft exhibited similar oscillations.

Figure 5.8 depicts the correlation manifolds respectively generated by the SR-DPE and the MR-DPE implementations during the bank-to-bank maneuver. While MR-DPE provided less pronounced improvements to the peak level of the correlation manifold, a sharper correlation manifold is noted from the cross-sections of the correlation manifolds shown in Fig. 5.9. As described earlier, this indicates MR-DPE was still able to deliver a higher level of measurement certainty in this high dynamic signal environment.

5.3 High-Terrain Environment

The third test point ("Sidewinder Transition" [45]) entailed some of the most challenging environments in which an airborne GPS receiver could be expected to operate. As shown in Fig. 5.10, the aircraft was traveling in Kern River Valley, California, at less than 300 meters above ground level, while on both sides the elevation of the mountainous terrain exceeded the altitude of the aircraft by as much as 1.5 kilometers. The signal challenge posed by the environment is also evident in Fig. 5.11.

To better illustrate the signal challenges experienced in this environment, the SNR history of the satellites in the last two minutes of the test point is
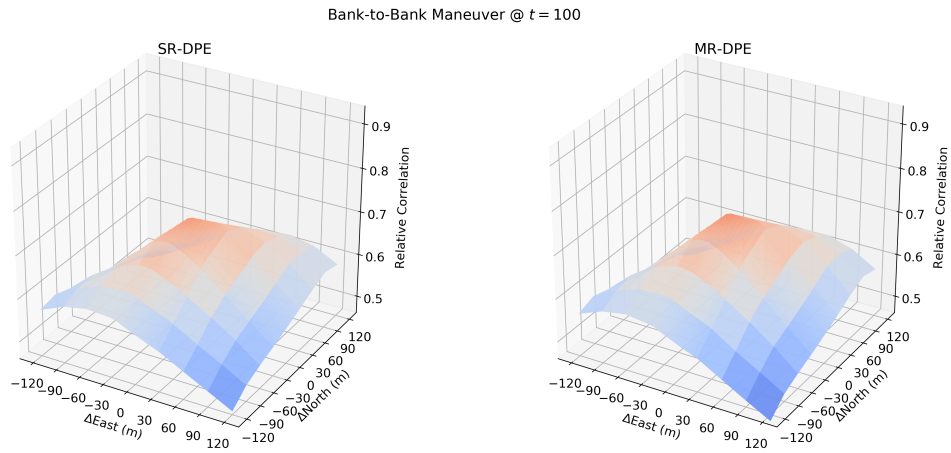
Figure 5.8: Correlation manifolds of SR-DPE and MR-DPE at $t = 100$ during the bank-to-bank maneuver. Both implementations experienced considerable decrease in correlation levels.
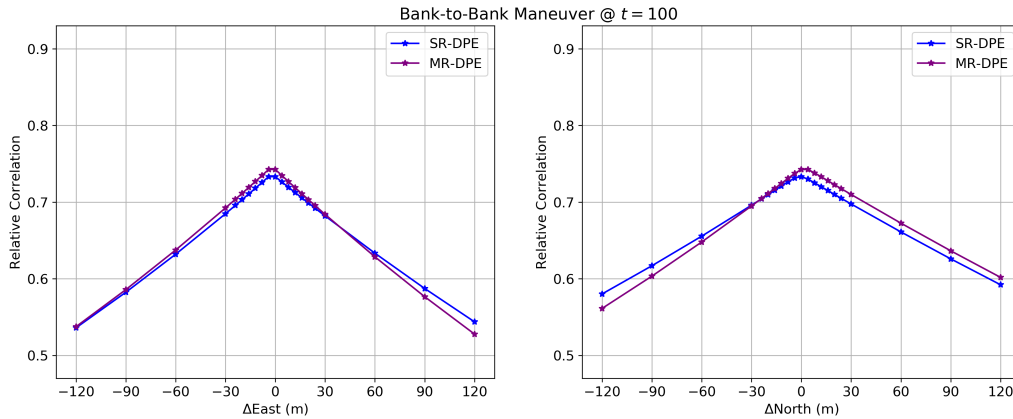

Figure 5.9: Cross-sections of the correlation manifolds at $t = 100$ during the bank-to-bank maneuver. Despite comparable levels of the correlation peaks, the overall manifold generated by MR-DPE remains noticeably sharper than its SR-DPE counterpart.
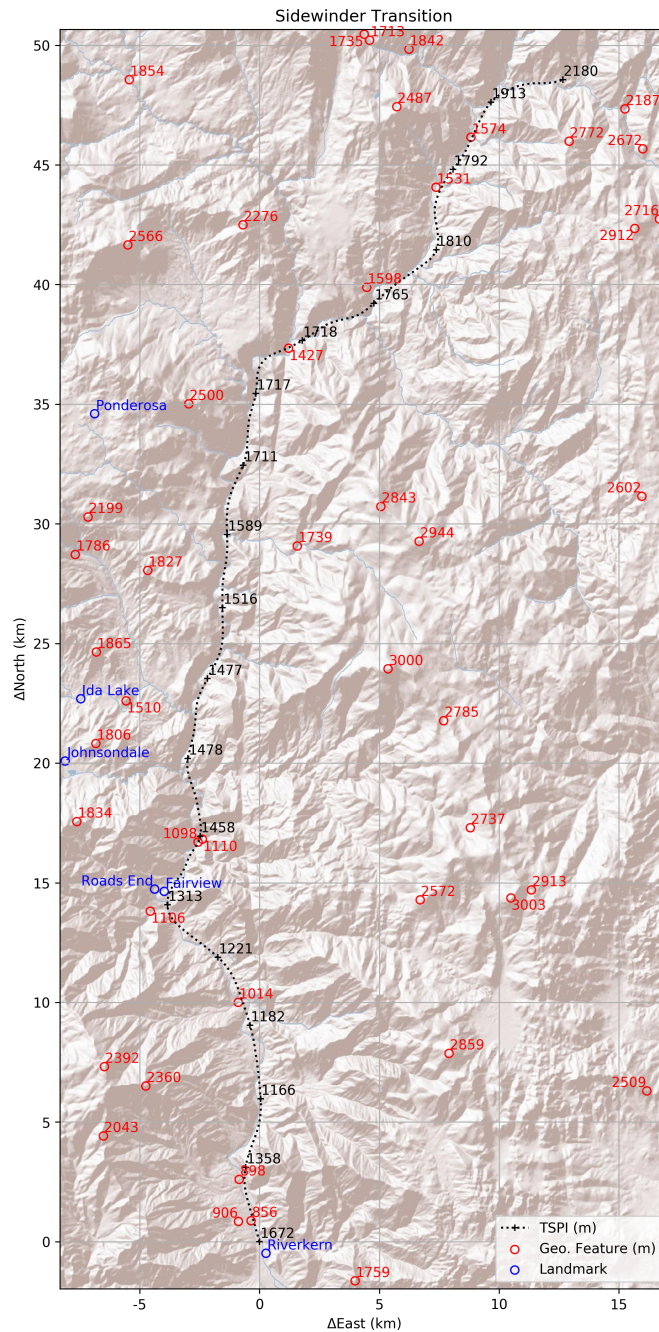
Figure 5.10: Ground track of the high-terrain test point, which traversed the Kern River Valley in California (terrain map: [44]). The black markers along the path indicate the altitude of the aircraft at a 30-second interval. Geographical features (summits, ridges and valleys) [46] and their corresponding elevations in meters are marked in red.

Figure 5.11: Side view from the flight test aircraft during Sidewinder Transition, deep inside Kern River Valley

shown in Fig. 5.12. Most notably, the SNRs of PRN 4, 11, 14, 16 and 26 experienced a simultaneous decrease around $t = 410$, and again around $t = 450$. An examination of the elevations and the azimuths of the four satellites at the time, as shown in Fig. 5.13, reveals that they were concentrated on the east side of the aircraft and their elevations were all below 45 degrees. Further study of the area revealed a cluster of high-elevation geographical features to the east of the flight path during the same period of time, corroborating the presence of signal masking effects.

Figure 5.14 presents the correlation manifolds generated by the SR-DPE and the MR-DPE implementations at $t = 450$, when multiple satellites were undergoing masking effects as indicated in Fig. 5.12. Both correlation manifolds bear considerably lower correlation levels when compared with the two previous test points. Nonetheless, both Fig. 5.14 and the cross-sections thereof, shown in Fig. 5.15, indicate that MR-DPE was successful in yielding a higher correlation peak and a sharper correlation manifold. This is consistent with our theory that MR-DPE is able to deliver a more advantageous performance in challenging signal environments.
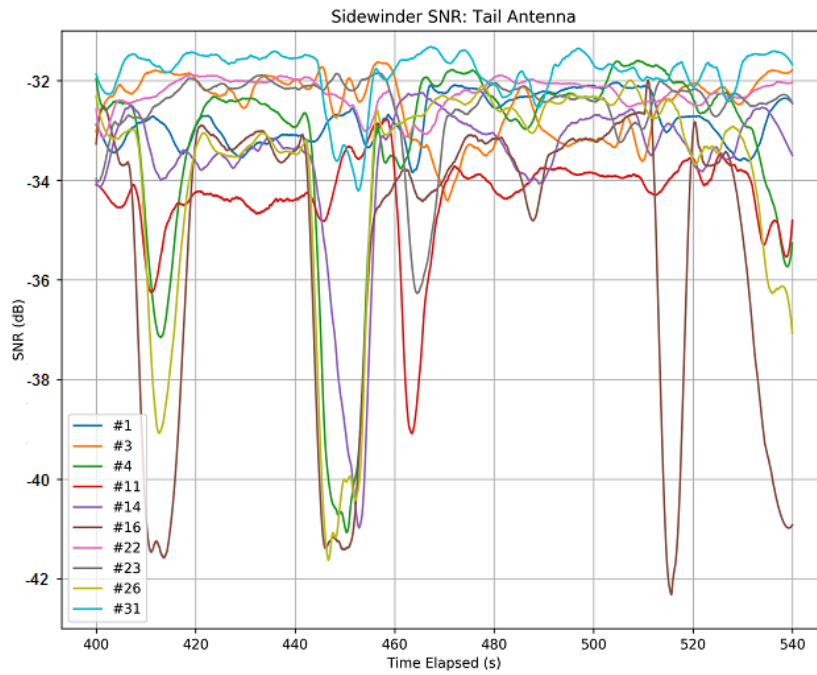
Figure 5.12: Multiple satellites experienced simultaneous reductions in SNR values during the Sidewinder Transition test point.
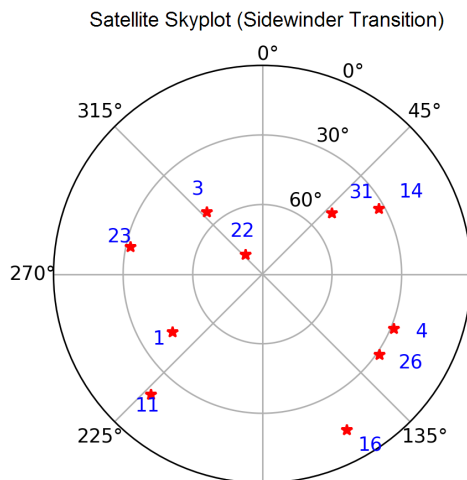

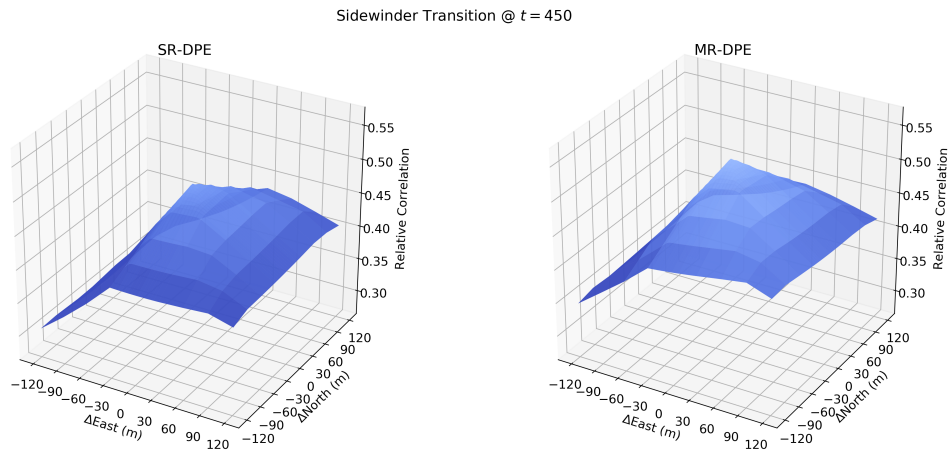Figure 5.13: Satellite skyplot of the Sidewinder Transition test point

Figure 5.14: Correlation manifolds of SR-DPE and MR-DPE at $t = 450$ during the Sidewinder Transition test point. Note that even though both correlation manifolds bore significantly lower peaks than before, a higher correlation level was still achieved by MR-DPE.
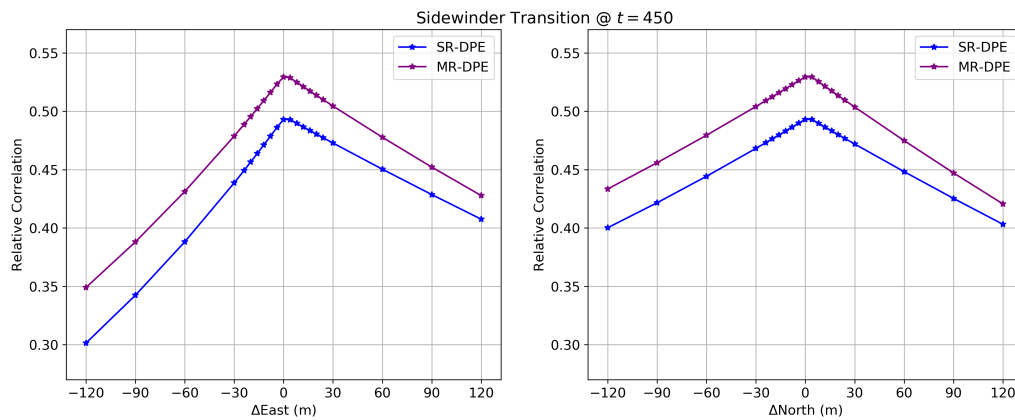

Figure 5.15: Cross-sections of the correlation manifolds at $t = 450$ during the Sidewinder Transition test point. Note the higher, sharper peak yielded from the MR-DPE when compared with SR-DPE.

CHAPTER 6

CONCLUSION AND FUTURE WORK

To summarize, we have presented a novel Multi-Receiver Direct Position Estimation (MR-DPE) architecture for aerial GPS receivers and highlighted the advantages of MR-DPE in degraded signal environments. We have formulated MR-DPE as a maximum-likelihood (ML) estimation problem and accordingly identified the key novelties of MR-DPE, including the ML-based attitude estimation algorithm and the SNR-based weighting during the fusion of the measurements.

A practical MR-DPE algorithm was then introduced and implemented with software-defined radio. This implementation was validated through a series of flight tests on a fixed-wing aircraft. A series of preliminary analyses were performed on the data collected to ensure the conceptual validity of MR-DPE. This work hence lays the foundation for future work on the quantitative examination on MR-DPE. In particular, statistical tools can be deployed to determine the accuracy of MR-DPE under the various flight profiles that have been explored in this thesis.

REFERENCES

[1] Global Positioning Systems Directorate, "Systems engineering and integration interface specification IS-GPS-200," 2015.

[2] J. Beser and B. W. Parkinson, "The application of NAVSTAR differential GPS in the civilian community," *Navigation*, vol. 29, no. 2, pp. 107–136, June 1982.

[3] J. T. Eck, T. L. Bristol, and J. J. Hickey, "Nextgen priorities joint implementation rolling plan 2017-2019 executive report," Sep. 2016. [Online]. Available: https://www.faa.gov/nextgen/media/NG_Priorities_Joint_Implementation_Plan.pdf

[4] P. Ward, "The natural measurements of a GPS receiver," in *Proceedings of the 51st Annual Meeting of The Institute of Navigation*, Colorado Springs, CO, June 1995, pp. 67–85.

[5] P. Misra and P. Enge, *Global Positioning System*. Ganga-Jamuna Press, 2006.

[6] J. J. Spilker, "Vector delay lock loop processing of radiolocation transmitter signals," US Patent 5,398,034, Mar. 14, 1995.

[7] G. X. Gao, M. Sgammini, M. Lu, and N. Kubo, "Protecting GNSS receivers from jamming and interference," *Proceedings of the IEEE*, vol. 104, no. 6, pp. 1327–1338, June 2016.

[8] R. D. J. Van Nee, "Spread-spectrum code and carrier synchronization errors caused by multipath and interference," *IEEE Transactions on Aerospace and Electronic Systems*, vol. 29, no. 4, pp. 1359–1365, Oct. 1993.

[9] R. L. Fante and J. J. Vaccaro, "Evaluation and reduction of multipath-induced bias on GPS time-of-arrival," *IEEE Transactions on Aerospace and Electronic Systems*, vol. 39, no. 3, pp. 911–920, July 2003.

[10] S. H. Kong, "Statistical analysis of urban GPS multipaths and pseudo-range measurement errors," *IEEE Transactions on Aerospace and Electronic Systems*, vol. 47, no. 2, pp. 1101–1113, Apr. 2011.

[11] J. F. McLellan, J. Schleppe, D. McLintock, and G. Deren, "GPS/barometry height-aided positioning system," in *Proceedings of 1994 IEEE Position, Location and Navigation Symposium - PLANS '94*, Las Vegas, NV, Apr. 1994, pp. 369–375.

[12] J. McDonald and J. Kendrick, "Benefits of tightly coupled GPS/IRS for RNP operations in terrain challenged airports," in *2008 IEEE/ION Position, Location and Navigation Symposium*, Monterey, CA, Apr. 2008, pp. 294–303.

[13] P. Closas, C. Fernández-Prades, and J. A. Fernández-Rubio, "Maximum likelihood estimation of position in GNSS," *IEEE Signal Processing Letters*, vol. 14, no. 5, pp. 359–362, May 2007.

[14] R. DiEsposti, "GPS PRN code signal processing and receiver design for simultaneous all-in-view coherent signal acquisition and navigation solution determination," in *Proceedings of the 2007 National Technical Meeting of The Institute of Navigation*, San Diego, CA, Jan. 2007, pp. 91–103.

[15] P. Axelrad, B. K. Bradley, J. Donna, M. Mitchell, and S. Mohiuddin, "Collective detection and direct positioning using multiple GNSS satellites," *Navigation*, vol. 58, no. 4, pp. 305–321, Dec. 2011.

[16] A. Weiss, "Direct position determination of narrowband radio frequency transmitters," *IEEE Signal Processing Letters*, vol. 11, no. 5, pp. 513–516, May 2004.

[17] P. Closas and A. Gusi-Amigo, "Direct position estimation of GNSS receivers: Analyzing main results, architectures, enhancements, and challenges," *IEEE Signal Processing Magazine*, vol. 34, no. 5, pp. 72–84, Sep. 2017.

[18] P. Closas, C. Fernandez-Prades, and J. A. Fernandez-Rubio, "Cramér-Rao Bound analysis of positioning approaches in GNSS receivers," *IEEE Transactions on Signal Processing*, vol. 57, no. 10, pp. 3775–3786, Oct. 2009.

[19] O. Bialer, D. Raphaeli, and A. J. Weiss, "Maximum-likelihood direct position estimation in dense multipath," *IEEE Transactions on Vehicular Technology*, vol. 62, no. 5, pp. 2069–2079, June 2013.

[20] J. Liu, H. Yin, X. Cui, M. Lu, and Z. Feng, "A direct position tracking loop for GNSS receivers," in *Proceedings of the 24th International Technical Meeting of The Satellite Division of The Institute of Navigation (ION GNSS+ 2011)*, Portland, OR, Sep. 2011, pp. 3634–3643.

[21] J. Liu, M. Lu, Z. Feng, and X. Cui, "Direct position tracking loop based on linearised signal model for global navigation satellite system receivers," *IET Radar, Sonar & Navigation*, vol. 7, no. 7, pp. 789–799, Aug. 2013.

[22] P. Closas, C. Fernández-Prades, J. Fernández-Rubio et al., "Evaluation of GNSS direct position estimation in realistic multipath channels," in *Proceedings of the 28th International Technical Meeting of The Satellite Division of The Institute of Navigation (ION GNSS+ 2015)*, Tampa, FL, Sep. 2015, pp. 3693–3701.

[23] Y. Ng and G. X. Gao, "Mitigating jamming and meaconing attacks using direct GPS positioning," in *2016 IEEE/ION Position, Location and Navigation Symposium (PLANS)*, Savannah, GA, Apr. 2016.

[24] J. J. Brewer, "The differential vector phase-locked loop for Global Navigation Satellite System signal tracking," Ph.D. dissertation, Air Force Institute of Technology, Wright-Patterson AFB, OH, June 2014.

[25] T. Lin, J. T. Curran, C. O'Driscoll, and G. Lachapelle, "Implementation of a navigation domain GNSS signal tracking loop," in *Proceedings of the 24th International Technical Meeting of The Satellite Division of The Institute of Navigation (ION GNSS+ 2011)*, Portland, OR, Sep. 2011, pp. 3644–3651.

[26] Y. Ng, "Improving the robustness of GPS direct position estimation," M.S. thesis, University of Illinois at Urbana-Champaign, Urbana, IL, Dec. 2016. [Online]. Available: http://hdl.handle.net/2142/95250

[27] A. Shetty and G. X. Gao, "Measurement level integration of multiple low-cost GPS receivers for UAVs," in *Proceedings of the 2015 International Technical Meeting of The Institute of Navigation*, Dana Point, CA, Jan. 2015, pp. 26–28.

[28] Y. Ng and G. X. Gao, "Advanced multi-receiver vector tracking for positioning a land vehicle," in *Proceedings of the 28th International Technical Meeting of The Satellite Division of The Institute of Navigation (ION GNSS+ 2015)*, Tampa, FL, Sep. 2015, pp. 3148–3155.

[29] Y. Ng and G. Gao, "GNSS multireceiver vector tracking," *IEEE Transactions on Aerospace and Electronic Systems*, vol. 53, no. 5, pp. 2583–2593, Oct. 2017.

[30] G. Lu, G. Lachapelle, M. E. Cannon, and B. Vogel, "Performance analysis of a shipborne gyrocompass with a multi-antenna GPS system," in *Proceedings of 1994 IEEE Position, Location and Navigation Symposium - PLANS '94*, Las Vegas, NV, Apr. 1994, pp. 337–343.

[31] L. Heng, J. J. Makela, A. D. Dominguez-Garcia, R. B. Bobba, W. H. Sanders, and G. X. Gao, "Reliable gps-based timing for power systems: A multi-layered multi-receiver architecture," in *2014 Power and Energy Conference at Illinois (PECI)*, Champaign, IL, Feb. 2014, pp. 1–7.

[32] S. Y. Lin and Z. Jiang, "GPS all in view time comparison using multi-receiver ensemble," in *2017 Joint Conference of the European Frequency and Time Forum and IEEE International Frequency Control Symposium (EFTF/IFC)*. Besançon, France: IEEE, July 2017.

[33] *Annex 10 to the Convention on International Civil Aviation*, 6th ed., International Civil Aviation Organization, Montreal, Québec, Canada, July 2006.

[34] A. G. Blackstock, J. DeMonte IV, P. J. Highland, M. S. Brodie, and J. P. Wilder, "Demonstration of aircraft state determination with blended solution of multiple GPS receivers: Project GRIFFIN," Edwards AFB, CA, June 2017.

[35] A. H.-P. Chu and G. X. Gao, "Multi-receiver direct position estimation tested on a full-scale fixed-wing aircraft," in *Proceedings of the 30th International Technical Meeting of The Satellite Division of The Institute of Navigation (ION GNSS+ 2017)*, Portland, OR, Sep. 2017, pp. 3761–3766.

[36] P. Closas, C. Fernandez-Prades, and J. A. Fernkndez-Rubiot, "ML estimation of position in a GNSS receiver using the SAGE algorithm," in *IEEE International Conference on Acoustics, Speech and Signal Processing - ICASSP '07*, vol. 3. Honolulu, HI: IEEE, Apr. 2007, pp. 1045–1048.

[37] J. W. Cheong, J. Wu, A. G. Dempster, and C. Rizos, "Assisted-GPS based snap-shot GPS receiver with FFT-accelerated collective detection: Time synchronisation and search space analysis," in *Proceedings of the 25th International Technical Meeting of The Satellite Division of The Institute of Navigation (ION GNSS+ 2012)*, Nashville, TN, Sep. 2012.

[38] E. Wycoff and G. X. Gao, "A Python software platform for cooperatively tracking multiple GPS receivers," in *Proceedings of the 27th International Technical Meeting of The Satellite Division of The Institute of Navigation (ION GNSS+ 2014)*, Tampa, FL, Sep. 2014, pp. 1417–1425.

[39] *SA.45s Chip-Scale Atomic Clock Options 001 and 003*, C ed., Microsemi Corporation, Aliso Viejo, CA, Apr. 2018.

[40] J. Shockley and D. Ruff, "TSPI vs. reference: What's the difference?" in *2008 U.S. Air Force T&E Days*. Los Angeles, CA: American Institute of Aeronautics and Astronautics, Feb. 2008.

[41] M. Veth, R. C. Anderson, F. Webber, and M. Nielsen, "Tightly-coupled INS, GPS, and imaging sensors for precision geolocation," Wright-Patterson AFB, OH, Jan. 2008.

[42] Honeywell International Inc, *HG1700 Inertial Measurement Unit*, Phoenix, AZ, 2016.

[43] Google Maps Elevation API. [Online]. Available: https://developers.google.com/maps/documentation/elevation

[44] Basemap Source: Esri, DigitalGlobe, GeoEye, i-cubed, USDA FSA, USGS, AEX, Getmapping, Aerogrid, IGN, IGP, swisstopo, and the GIS User Community. [Online]. Available: http://server.arcgisonline.com/arcgis/rest/services

[45] "Edwards Air Force Base Instruction 13-100," 412 OSS/OSA, Oct. 2016.

[46] U.S. Board on Geographic Names, https://geonames.usgs.gov, accessed: 2018-05-28.